Experimental investigation on the evolution of the modulation instability with dissipation

Y. Ma[1]†, **G. Dong**[1], **M. Perlin**[2], **X. Ma**[1] **and G. Wang**[3]

[1] State Key Laboratory of Coastal and Offshore Engineering, Dalian University of Technology, Dalian, 116024, China

[2] Department of Naval Architecture and Marine Engineering, University of Michigan, Ann Arbor, MI 48109, USA

[3] School of Harbor, Coastal and Offshore Eningeering, Hohai University, Nanjing, 210098, China

An experimental investigation focusing on the effect of dissipation on the evolution of the Benjamin–Feir instability is reported. A series of wave trains with added sidebands, and varying initial steepness, perturbed amplitudes and frequencies, are physically generated in a long wave flume. The experimental results directly confirm the stabilization theory of Segur *et al.* (*J. Fluid Mech.*, vol. 539, 2005, pp. 229–271), i.e. dissipation can stabilize the Benjamin–Feir instability. Furthermore, the experiments reveal that the effect of dissipation on modulational instability depends strongly on the perturbation frequency. It is found that the effect of dissipation on the growth rates of the sidebands for the waves with higher perturbation frequencies is more evident than on those of waves with lower perturbation frequencies. In addition, numerical simulations based on Dysthe's equation with a linear damping term included, which is estimated from the experimental data, can predict the experimental results well if the momentum integral of the wave trains is conserved during evolution.

Key words: ocean processes, surface gravity waves, wind–wave interactions

---

1. Introduction

Following the landmark work of Benjamin & Feir (1967), it is now well known that deep-water gravity waves are unstable to small perturbations and that the unstable disturbances grow exponentially as the wave trains evolve. Hereafter, this phenomenon is called the Benjamin–Feir instability or the modulational instability. At about the same time, Zakharov (1968) demonstrated that the evolution of narrowband wave trains is well described by the nonlinear Schrödinger (NLS) equation. Over the decades since, much progress has been made in the understanding of this phenomenon by both theoretical and experimental approaches, and it has contributed greatly to the knowledge of deep-water waves. Detailed surveys on this topic can be found in the review articles of Yuen & Lake (1980) and Hammack & Henderson (1993).

Recently, Segur *et al.* (2005) have proven theoretically that, even if the dissipation is weak, it can prevent the instability of wave trains with small and moderate amplitudes; they also performed laboratory experiments to confirm their theory. (In fact, Mei & Hancock 2003 have obtained a similar result using the NLS equation with an empirical

† Email address for correspondence: yuxma@126.com

complex dissipation term.) The conclusion of Segur *et al.* (2005) was somewhat surprising as in the previous experiments of Benjamin (1967) and Lake *et al.* (1977), the presence of dissipation only reduced the growth rate of the unstable disturbances.

Subsequent to the work of Segur *et al.* (2005), many similar studies have been conducted. However these studies were based primarily on theoretical and numerical approaches. For example, the stabilization theory for long-time wave train evolution was confirmed by Wu, Liu & Yue (2006) using a fully nonlinear numerical model. Canney & Carter (2007) added a linear dissipation term to the NLS equation, to Dysthe's equation, and to the band-modified NLS equation (Trulsen & Dysthe 1996) respectively, and found that any finite amount of dissipation bounds the growth of the sidebands of plane waves. Carter & Contreras (2008) showed that with the presence of dissipation, the solution of the NLS equation is linearly stable, though perturbations may grow a finite amount. Islas & Schober (2011) showed that the presence of damping can prevent the development of freak waves based on Dysthe's equation. Kharif *et al.* (2010) combined the effects of wind and dissipation in the NLS equation and demonstrated that this combination has a cumulative effect on the modulation evolution. This aggregate effect has been shown using a fully nonlinear wave model in their subsequent work (Touboul & Kharif 2010).

To date, though many previous experimental studies (Melville 1982; Tulin & Waseda 1999; Waseda & Tulin 1999; Chiang & Hwung 2007; Hwung, Chiang & Hsiao 2007) on the modulational instability have been carried out, and much progress has been made, there are but a few experiments focusing on the effect of dissipation on the Benjamin–Feir instability. Segur *et al.* (2005) presented only a few cases. And very recently, Henderson, Segur & Carter (2010) experimentally demonstrated the stability of bi-periodic patterns of waves on deep water when dissipation was included. However they had a relatively short facility, thus very short waves (wavelengths of 0.14 m) were used. The lack of experiments to further verify the stabilization theory is the primary motivation of this study. To our knowledge, the results presented here represent the first experiments to consider initially perturbed wave trains with varying steepness and added sidebands, to provide quantitative evidence of the effect of dissipation on the modulational instability in deep water.

In this study, we have performed detailed experiments by varying initial wave steepness and added sidebands so that we could quantitatively examine the theory of Segur *et al.* (2005). However, due to the limitation of the present flume ($\sim$50 m of usable length), the main focus of this study is the effect of dissipation on the initial stage of the modulational evolution.

The paper is arranged as follows. In §2 the experimental procedure and data analysis are described in detail. Experimental results and some numerical simulations based on Dysthe's equation are presented in §3. A discussion of the results on the growth of sidebands is included in §4. Lastly, conclusions are advanced in §5.

2. Description of the experiment

2.1. *Experimental setup*

The experiments are conducted in a wave–current flume located at the State Key Laboratory of Coastal and Offshore Engineering, Dalian University of Technology, Dalian, China. The flume is 65 m long, 2 m wide and 1.8 m deep. The detailed experimental setup is shown in figure 1. In this flume, both waves and currents can be generated; however only waves are generated in this study. The flume is equipped with a servo-motor-driven piston-type wavemaker with $x = 0$ m defined as
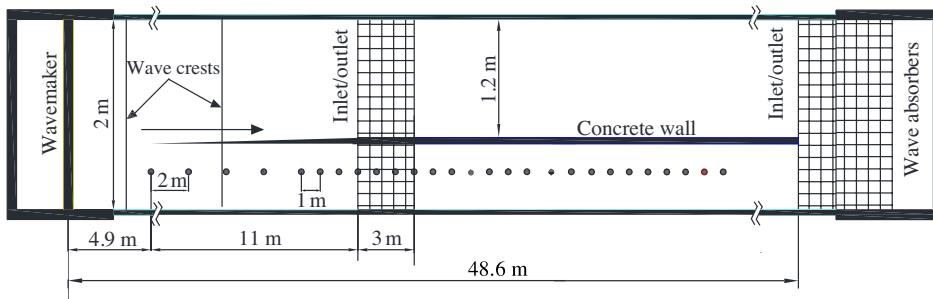
FIGURE 1. (Colour online) Experimental set-up (not to scale).

the mean position of the wavemaker. At the other end of the flume, wave absorbers are installed to mitigate wave reflection. Prior experiments have shown that the reflection coefficient is only ∼5 % for 1 Hz waves; thus we neglect its effect. In a physical wave flume, viscous dissipation due to sidewalls is ubiquitous (Banner & Peirson 2007; Tian, Perlin & Choi 2010). To increase the energy dissipation by the sidewalls for this investigation, from $x = 8.9$ m onward, a narrower width flume is used; a surface-ground concrete wall separates the flume longitudinally into two sections with widths of 0.8 and 1.2 m with the surface ground to give a condition similar to the glass wall and thus help retain a two-dimensional flow. The narrower 0.8 m wide section is chosen as the working section. By using the narrower side of the flume, the likelihood of retaining two-dimensionality of the wave field is increased.

The water surface elevations are recorded simultaneously with 36 capacitance wave gauges, which are shown by filled circles in figure 1. For $x < 12.9$ m, the distance between the wave gauges is 2 m; for the remainder of the flume, the gauge spacing is decreased to 1 m. The absolute accuracy of these gauges is of the order of ±1 mm. Before initiating any measurements, the gauges are examined for soundness, cleaned if necessary, and then calibrated. All experiments are repeated three times to ensure the repeatability of the entire system and to provide an indication of the error. Between experiments at least 15 min is allowed to elapse to ensure a calm water surface. The data acquisition system is PC based with multiple channels, and was developed by Beijing Hydraulic Research Institute. The water surface elevations are sampled with frequency 50 Hz, and the duration of each record is 163.84 s.

2.2. Wave group generation

Wave trains with imposed sidebands, or so-called 'seeded' waves (Tulin & Waseda 1999), are chosen. This method ensures that the background noise is suppressed significantly (Tulin & Waseda 1999). The imposed sideband wave train is as follows:

$$\eta = a_c \cos(2\pi f_c t) + a_+ \cos(2\pi f_+ t + \varphi_+) + a_- \cos(2\pi f_- t + \varphi_-), \quad (2.1)$$

$$f_\pm = f_c \pm \Delta f, \quad (2.2)$$

where a_c, a_+ and a_- are the amplitudes of the carrier, upper sideband and lower sideband respectively, f_c, f_+ and f_- are the corresponding cyclic frequencies, Δf is the frequency difference between the carrier wave and its sidebands, and φ_+ and φ_- are the initial phase differences between the sidebands and the carrier wave, which are set to $-\pi/4$ in the generation signal, to provide the maximum growth rate (Benjamin & Feir 1967). Here the initial steepness ε and the amplitude a_0 of the wave trains are

Case	f_c (Hz)	ε	Δf (Hz)	a_-/a_c	a_+/a_c	β_x	δ	BFI	ΔE (%)	σ_e (m^{-1})
SB1	1.0	0.115	0.05	0.058	0.092	0.0056	0.44	4.6	0.33	0.0058
SB2	1.0	0.115	0.075	0.044	0.064	0.0065	0.65	3.1	0.34	0.0067
SB3	1.0	0.115	0.1	0.041	0.047	0.0061	0.87	2.3	0.31	0.0057
SB4	1.0	0.115	0.125	0.043	0.046	−0.0005	1.09	1.8	0.36	0.0062
SB5	1.0	0.157	0.05	0.061	0.084	0.0097	0.32	6.3	0.33	0.0059
SB6	1.0	0.157	0.075	0.044	0.073	0.0125	0.48	4.2	0.33	0.0064
SB7	1.0	0.157	0.1	0.047	0.045	0.0128	0.64	3.1	0.32	0.0068
SB8	1.0	0.157	0.125	0.051	0.047	0.0113	0.8	2.5	0.35	0.0072
SB9	1.0	0.157	0.15	0.041	0.045	0.0073	0.96	2.1	0.35	0.0061
SB10	1.0	0.157	0.175	0.038	0.069	0.0042	1.11	1.8	0.33	0.0056
SB11	1.0	0.115	0.125	0.079	0.117	—	1.09	1.9	0.33	0.0061
SB12	1.0	0.115	0.175	0.081	0.129	—	1.09	1.3	0.30	0.0063
SB13	1.0	0.157	0.125	0.191	0.204	—	1.11	2.5	0.31	0.0068
SB14	1.0	0.157	0.175	0.163	0.207	—	1.11	1.8	0.32	0.0065

TABLE 1. Wave parameters measured at the first location $x = 4.9$ m

defined as:

$$\varepsilon = k_c a_0, \tag{2.3}$$

$$a_0 = \sqrt{a_c^2 + a_+^2 + a_-^2}, \tag{2.4}$$

where k_c is the wavenumber of the carrier wave, which satisfies the deep-water dispersion relationship:

$$(2\pi f_c)^2 = g k_c. \tag{2.5}$$

To investigate fully the effect of dissipation on the modulational evolution of deep-water waves, wave trains with varying initial steepness, varying frequency and differing perturbation amplitude are chosen. The detailed wave parameters, which are determined from the measured data at the first location ($x = 4.9$ m), are shown in tables 1 and 2. Here, δ is a non-dimensional frequency parameter:

$$\delta = \Delta f / \varepsilon f_c. \tag{2.6}$$

When the value of δ is in the range 0–$\sqrt{2}$, the condition of the modulational instability is satisfied (Benjamin & Feir 1967). Janssen (2003) defined a parameter called the Benjamin–Feir index (BFI) to determine the instability onset:

$$\text{BFI} = \frac{2\varepsilon f_c}{\Delta f}. \tag{2.7}$$

According to Alber (1978) and in terms of Janssen's BFI, if BFI is larger than 1, the modulational instability develops along the wave propagation direction. In addition $\Delta E = (E_i - E_f)/E_i$ is the measured energy loss in the tank (presented as a percentage in table 1), where E_i and E_f are the measured energies at the initial and final measurement locations, with the wave energy E herein defined as:

$$E = \sum_{n=1}^{N} A_n^2. \tag{2.8}$$

Case	a_c (cm)	a_{+1} (cm)	a_{-1} (cm)	a_{+2} (cm)	a_{-2} (cm)
SB1	$-0.41 + 2.77i$	$0.08 + 0.24i$	$-0.137 - 0.02i$	$-0.006 + 0.05i$	$0.012 - 0.04i$
SB2	$-2.26 + 1.82i$	$0.006 + 0.18i$	$-0.08 - 0.086i$	$-0.026 + 0.01i$	$0.025 - 0.007i$
SB3	$-2.4 - 1.77i$	$-0.1 + 0.087i$	$0.083 - 0.077i$	$-0.011 - 0.012i$	$0.01 + 0.016i$
SB4	$0.78 - 2.85i$	$-0.13 - 0.014i$	$0.11 + 0.052i$	$0.0001 - 0.005i$	$-0.01 + 0.007i$
SB5	$2.98 - 2.53i$	$0.153 - 0.267i$	$0.04 + 0.20i$	$0.045 - 0.035i$	$-0.04 + 0.008i$
SB6	$-0.99 + 3.774i$	$0.036 + 0.276i$	$-0.157 - 0.001i$	$-0.024 + 0.045i$	$0.003 - 0.024i$
SB7	$2.28 - 3.16i$	$-0.04 - 0.164i$	$0.138 + 0.101i$	$-0.001 - 0.012i$	$-0.022 + 0.004i$
SB8	$0.348 - 3.836i$	$-0.165 - 0.068i$	$0.157 + 0.091i$	$-0.006 - 0.003i$	$-0.009 + 0.012i$
SB9	$-2.01 + 3.41i$	$0.077 + 0.16i$	$-0.11 - 0.09i$	$-0.01 - 0.0024i$	$0.02 - 0.006i$
SB10	$1.082 + 3.64i$	$-0.063 + 0.256i$	$0.088 + 0.073i$	$-0.007 + 0.019i$	$-0.011 - 0.011i$
SB11	$1.42 - 2.62i$	$0.133 - 0.32i$	$0.119 - 0.177i$	$0.028 - 0.021i$	$-0.012 + 0.021i$
SB12	$-2.601 + 1.33i$	$-0.11 - 0.59i$	$0.416 + 0.315i$	$0.028 + 0.106i$	$-0.002 - 0.036i$
SB13	$-2.604 - 2.643i$	$-0.36 - 0.32i$	$-0.146 - 0.196i$	$-0.036 - 0.041i$	$0.014 + 0.014i$
SB14	$3.41 + 1.621i$	$0.777 - 0.035i$	$0.173 + 0.496i$	$0.145 - 0.02i$	$-0.028 - 0.03i$

TABLE 2. The complex amplitudes measured at the first location $x = 4.9$ m

In this equation A_n is the measured amplitude of the nth Fourier mode while N represents the highest Fourier mode. For all experimental cases, the energy loss along the tank is nearly identical. The last column of table 1 presents the fitted decay parameter σ_e, which will be used as a linear damping term in Dysthe's equation (see § 3.2).

To reduce the effect of wave fronts, following Tulin & Waseda (1999), a finite ramp $e(t)$ is added at the beginning and the end of the wave generation signals:

$$e(t) = \begin{cases} \frac{1}{2}(1 - \cos(\pi t/\tau)), & 0 \leqslant t \leqslant \tau, \\ 1, & \tau < t \leqslant T - \tau, \\ \frac{1}{2}(1 - \cos(\pi(t - T)/\tau)), & T - \tau < t \leqslant T, \end{cases} \tag{2.9}$$

where τ is the ramp duration and T is the total duration of the signal.

2.3. *Data analysis method*

Wave spectra are used to examine the redistribution of energy across the frequency spectrum. In this study, wave spectra are obtained by fast Fourier transform (FFT), and then smoothed by the Hanning window. The frequency resolution of the spectra is $\sim$0.012 Hz, which is small enough to distinguish adjacent wave modes. The amplitudes, a_n, from the wave energy spectra are estimated as the square root of the energy of the spectral peaks by integrating the contributions from the neighbouring frequency bins as follows:

$$a_n^2 = \frac{1}{2}(A_{n-1}^2 + A_{n+1}^2) + A_n^2. \tag{2.10}$$

This method is used to help compensate for the leakage of the spectral energy due to the finite length of the time series record.

To study the initial sideband growth rate β_x, the following steps are implemented (Lake *et al.* 1977; Waseda & Tulin 1999). The calculated amplitudes of the sidebands $(a_\pm)$ are non-dimensionalized by the carrier wave amplitude (a_c). Next, the mean non-dimensional sideband amplitudes $\bar{a}$ are calculated by averaging the non-dimensional amplitudes of the upper and lower sidebands (a_+, a_-). Then, the mean non-dimensional sideband amplitudes $\bar{a}$ are plotted versus non-dimensional distance kx, and β_x is estimated through fitting the data to the model equation:

$$\bar{a}(kx) = \bar{a}(0) \exp(\beta_x kx), \tag{2.11}$$

using the least-squares method. Illustration of this method can be seen in figure 2, which indicates that it can estimate the sideband growth accurately. The estimated β_x for the weak modulated cases are shown in table 1.

3. Results

3.1. *Evolution of the measured results*

Figure 3 shows the evolution at the first and the last measurement locations of the surface elevations and the corresponding spectra for three initial weakly modified cases with $\varepsilon = 0.115$. We can see that the modulation has developed slightly downstream. In particular, as is evident from their spectra, there is almost no change in the wave train for Case SB4, which in fact has a similar theoretical growth rate to Case SB1. In these cases, though sideband amplitudes developed, the spectra at the end of the flume indicate that there is no apparent asymmetric growth of the lower and upper sidebands, which always was observed in experiments with large amplitudes
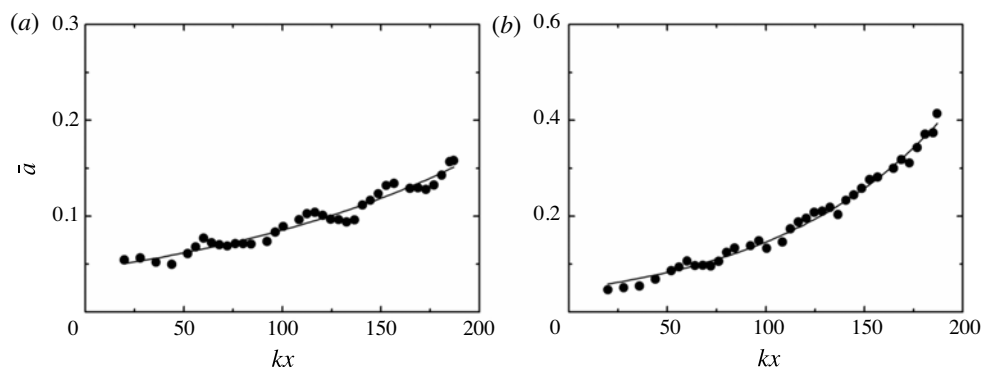
FIGURE 2. Illustration of the fitting of the non-dimensional amplitudes. Solid circles: measured non-dimensional amplitudes, curves: fitted results: (*a*) Case SB2, $\beta_x = 0.0065$; (*b*) Case SB8, $\beta_x = 0.0113$.

(Melville 1982; Tulin & Waseda 1999). It is noted that as the waves propagated, no sideband amplitude exceeded one quarter of the carrier wave amplitude (see figure 11). Thus, the $x = 4.9$ m and $x = 46.9$ m data presented in figure 3 are indicative of the downstream evolution.

The measured amplitude evolution of the lower and upper sidebands for the weakly perturbed cases with $\varepsilon = 0.115$ are shown in figure 4 (i.e. Cases SB1 to SB4, respectively). (Throughout this paper, these measured amplitudes are designated by '*a*' as in figure 4.) For the first three cases, the amplitudes of the sidebands oscillated, but in an increasing manner along the flume. However, no sideband grew to exceed even one quarter of the carrier wave (figure 11). Contrastingly, the sideband amplitudes for Case SB4 have not increased, but exhibited a slight tendency to decrease, even though the initial condition satisfied the onset criterion ($\delta < \sqrt{2}$) of the Benjamin–Feir instability. At the middle of the wave channel, about $x = 25$ m, the wave system of Case SB4 still satisfied the onset condition of the Benjamin–Feir instability ($a_c = 2.74$ cm, $a_- = 0.11$ cm, $a_+ = 0.13$ cm, $\varepsilon = 0.1106$, $\delta = 1.13$, BFI $= 1.77$). However, in the presence of sufficient dissipation, a modulational instability is not initiated, i.e. the waves are stabilized (Segur *et al.* 2005). As the theoretical growth rates of Cases SB1 and SB4 are similar (see figure 7 below), but the sideband evolution of the two cases is different, it appears that the effect of dissipation on the Benjamin–Feir instability depends on the perturbation frequencies. The cases with larger initial steepness also exhibited this phenomenon (see figure 6 below).

In figure 4 it is noted that the amplitudes of the oscillations exhibited constant fluctuation lengths, and are seemingly related to the perturbation frequencies. (A detailed discussion on this is presented in §4.) This phenomenon may be caused by fifth- or higher-order wave–resonant interactions, as they are not described by the fourth-order NLS equation (see the next section).

Figure 5 shows the measured surface elevations and the corresponding spectra for some initial weakly disturbed cases with a larger initial steepness ($\varepsilon = 0.157$). These cases exhibit an obvious development in both the time and the frequency domains. However, in these cases, no sideband amplitude grew to exceed the amplitude of the carrier wave (see figures 6 and 12), i.e. frequency downshift is not observed in these cases. Additionally, there is apparent development at a_{-n} and a_{+n} with frequencies ($f_c \pm n\delta f$) and $n > 1$, that automatically occurred in the evolution process as they also
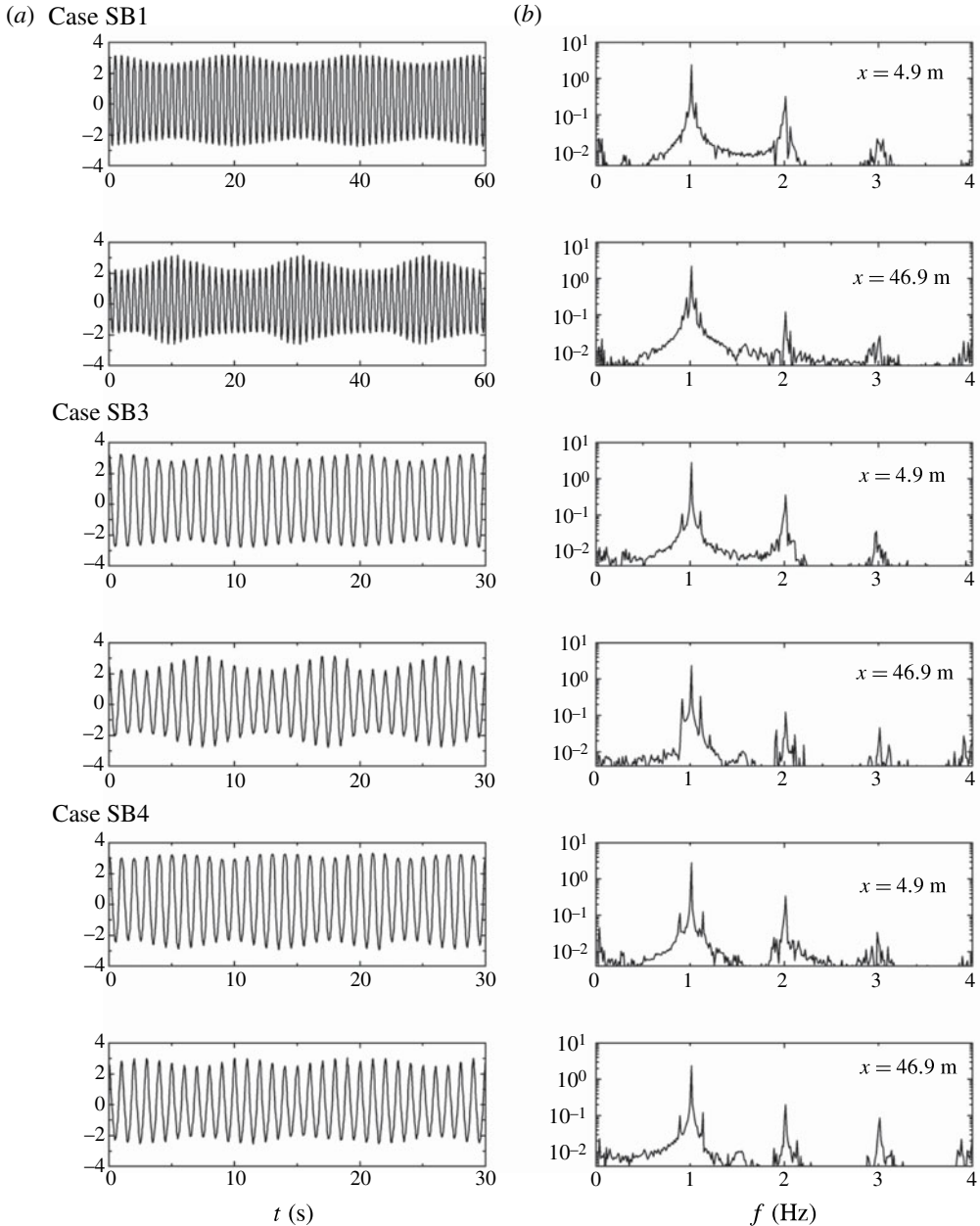
FIGURE 3. Measured surface elevations (*a*) and their corresponding spectra (*b*) for some initial weakly modified wave trains, $\varepsilon = 0.115$.

satisfied the onset of the modulational instability condition. However the development of these modes is not as obvious for the cases with higher perturbation frequency (Case SB14).

The evolution of the measured sidebands for the cases presented in figure 4 is clarified in figure 6. Noting the ordinate scale difference between figures 3 and 5, the
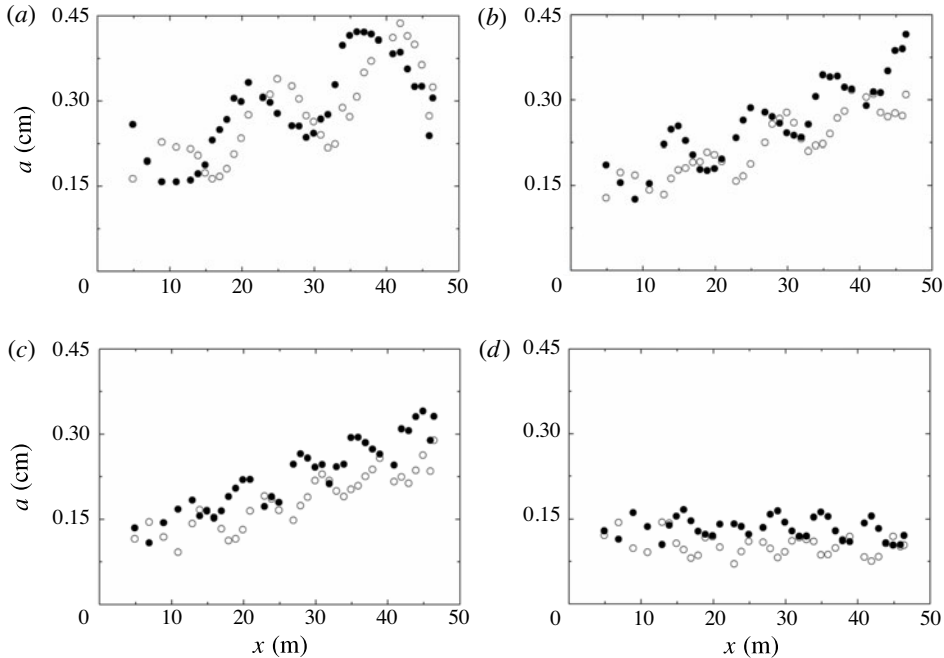
FIGURE 4. The evolution of the measured sidebands for the initial weakly perturbed cases with $\varepsilon = 0.115$; open circles: lower-sideband amplitudes; filled circles: upper-sideband amplitudes: (*a*) $\delta = 0.44$ (Case SB1); (*b*) $\delta = 0.65$ (Case SB2); (*c*) $\delta = 0.87$ (Case SB3); (*d*) $\delta = 1.09$ (Case SB4).

growth of the sideband amplitudes is more significant than those cases with smaller initial steepness. This is especially true for the Case SB10, which has a similar δ to Case SB4, where the sideband amplitudes increased downstream, even though the growth rate is not obvious, indicating that the stabilization effect can be mitigated by increasing the initial steepness. It is noted that the oscillation of the sidebands along the flume is not as obvious for these cases, as the oscillation amplitudes are small compared with the exponential growth of the sidebands.

The initial growth rates β_x estimated by (2.11) for the cases with weak perturbations are much smaller than the theoretical results (figure 7), indicating that the increase of the sidebands for these cases is bounded by dissipation (see figure 7). The above results show that the dissipation rates for all the cases are similar, but that the sidebands growth varies, indicating that the effect of dissipation on the modulational instability depends heavily on the modulational frequency. Moreover, the influence of dissipation on the modulational instability for a lower disturbance frequency is less than those cases with a higher disturbance frequency, even when they have a similar theoretical growth rate. The suppression effect on the growth rate of the sidebands is not evident for the wave trains with the smallest perturbed frequencies ($\Delta f = 0.05$ Hz). However, the evolution of the waves with perturbation frequencies close to the upper marginal frequency is depressed completely. In addition, it is noticed that discrepancies between the measured growth rate and the theory for the cases with larger steepness are more significant than those cases with smaller steepness, indicating that the effect of dissipation on larger waves is more evident than on smaller waves.
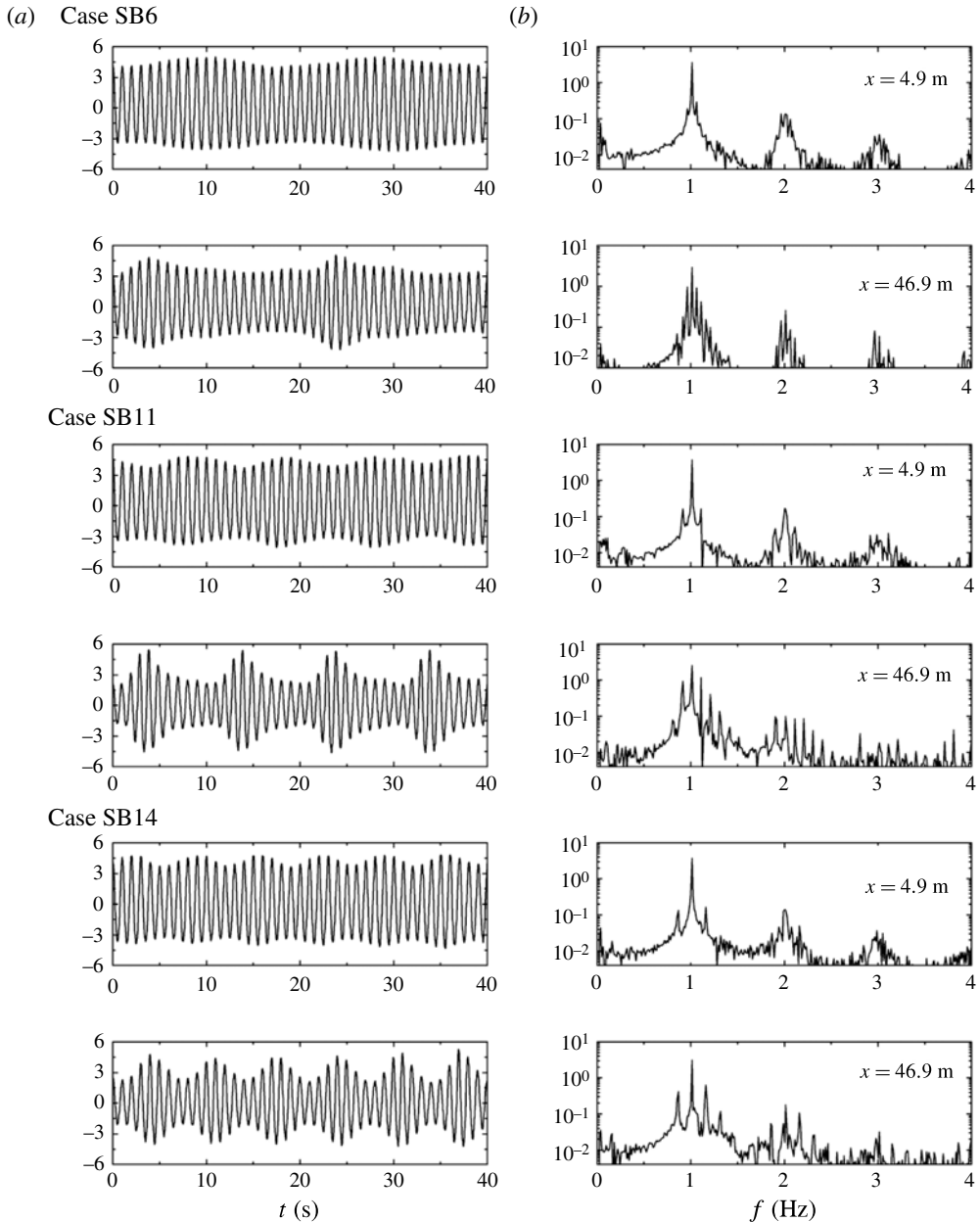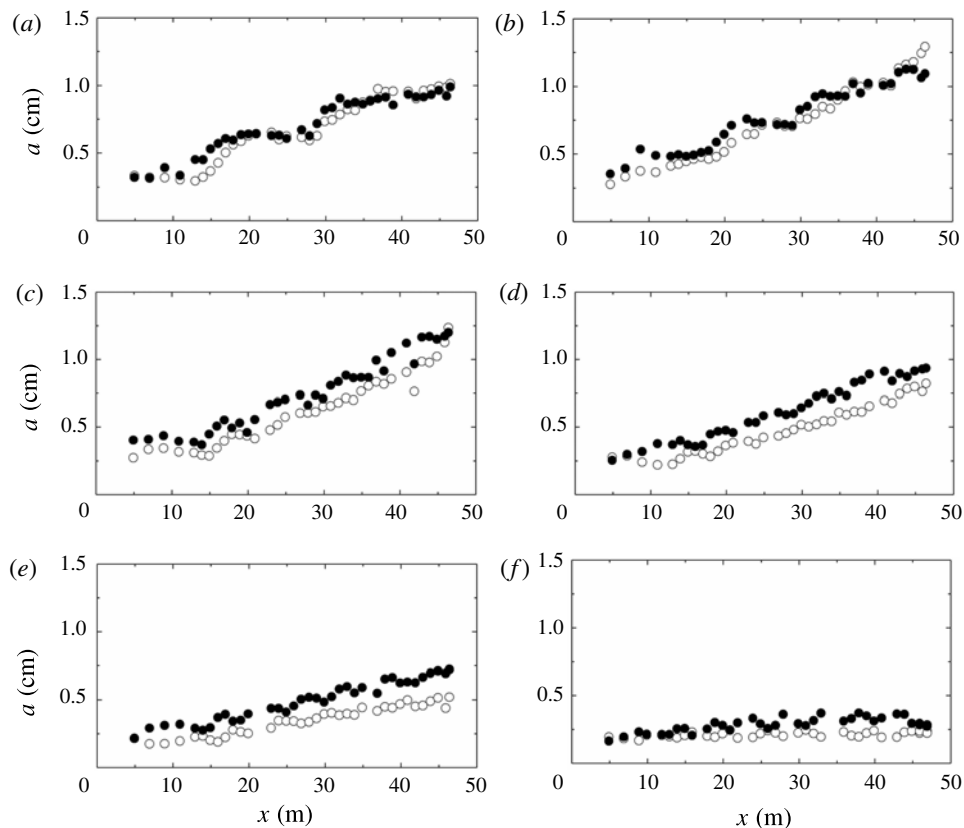
(*a*)   Case SB6   (*b*)

FIGURE 5. The measured surface elevations (*a*) and the corresponding spectra (*b*) for the initial weakly modified wave trains, $\varepsilon = 0.157$.

The stabilization effect on the modulation instability can be mitigated by increasing the initial steepness (by comparing figures 4*d* and 6*d*) suggesting that increasing the initial sideband amplitudes may remove the effect of stabilization. Likewise, the sideband-amplitude evolution for cases with larger initial perturbations are shown in figures 8 and 9 (note that the corresponding cases with smaller initial perturbations are totally suppressed presumably by dissipation, and that these wave trains are

FIGURE 6. Evolution of the measured sidebands for an initially weak perturbation, $\varepsilon = 0.157$; open circles: lower-sideband amplitudes; filled circles: upper-sideband amplitudes. (*a*) $\delta = 0.32$ (Case SB5), (*b*) $\delta = 0.48$ (Case SB6), (*c*) $\delta = 0.64$ (Case SB7), (*d*) $\delta = 0.8$ (Case SB8), (*e*) $\delta = 0.96$ (Case SB9), (*f*) $\delta = 1.11$ (Case SB10).

stabilized). For these cases the sideband amplitudes do not decrease, but in fact increase downstream, indicating that instability has developed further. However, it is noticed that the growth of the lower sidebands is not as evident as is that of the upper sidebands, especially at the later stage of the modulation (see figure 9). This is very different from the previous laboratory results (Tulin & Waseda 1999; Hwung *et al.* 2007) in which the dissipation was negligible due to the large width of their tanks. The previous experiments also have shown the asymmetric evolution between the lower and the upper sidebands in the later stage of evolution, but in those experiments the lower sidebands were always larger than the upper sidebands, and eventually frequency downshift occurred.

3.2. *Comparison between the experiments and numerical results*

It is well known that the evolution of weakly nonlinear deep-water waves with narrow-band spectra obeys the NLS equations (Zakharov 1968; Lake *et al.* 1977). Dysthe (1979) derived a modified NLS with a correction term for broader bandwidths. Even though this modified NLS equation does not have a Hamiltonian structure (Gramstad & Trulsen 2011), it is used widely to model the evolution of the modulational
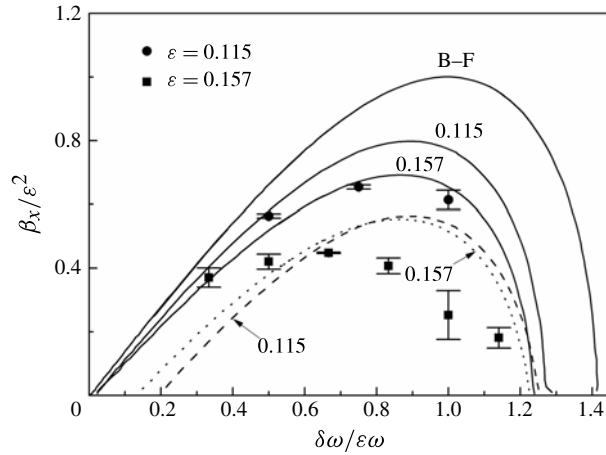
FIGURE 7. The initial growth rates of the measured sideband amplitudes. The upper solid curve is the theoretical result of Benjamin & Feir (1967); the lower two solid curves are the predictions based on the reduced fourth-order interaction equation (Krasitskii 1994) for $\varepsilon = 0.115$ and 0.157. The dotted line is the prediction by Krasiskii's equation minus the mean measured decay rate for the cases with $\varepsilon = 0.115$, and the dashed line that for the cases with $\varepsilon = 0.157$. The experimental data with error bars are also shown on the figure.
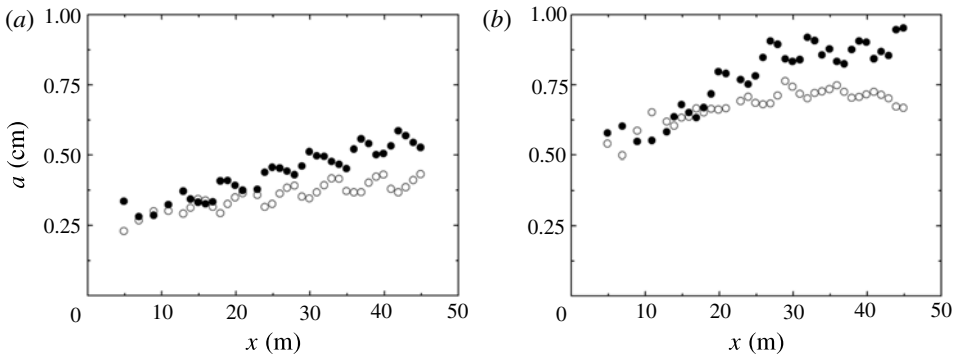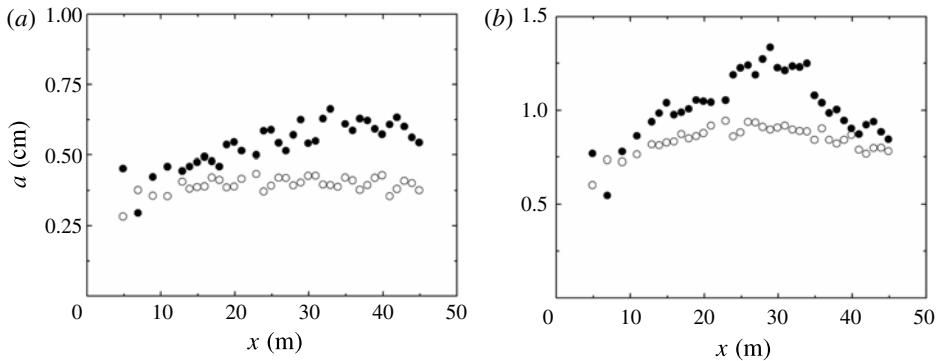

FIGURE 8. Evolution of the measured sideband amplitudes for cases with $\varepsilon = 0.115$ and larger initial amplitude modulation; open circles: lower-sideband amplitudes; filled circles: upper-sideband amplitudes. (*a*) Case SB11; (*b*) Case SB13.

instability (Lo & Mei 1985; Islas & Schober 2011). Dysthe's equation with a linear damping term can be written as:

$$\frac{\partial A}{\partial t} + \frac{\omega_0}{2k_0}\frac{\partial A}{\partial x} + i\frac{\omega_0}{8k_0^2}\frac{\partial^2 A}{\partial x^2} + \frac{i}{2}\omega_0 k_0^2|A|^2 A - \frac{\omega_0}{16k_0^3}\frac{\partial^3 A}{\partial x^3} - \frac{\omega_0 k_0}{4}A^2\frac{\partial A^*}{\partial x}$$
$$\frac{3\omega_0 k_0}{2}|A|^2\frac{\partial A}{\partial x} + ik_0 A\frac{\partial \phi}{\partial x}\bigg|_{z=0} + \sigma A = 0, \tag{3.1}$$

where A is the complex amplitude of the wave, A^* is the complex conjugate of A, ω_0 is the angular frequency of the carrier wave, k_0 is the wavenumber, ϕ is the potential

FIGURE 9. Evolution of the measured sideband amplitudes for cases with $\varepsilon = 0.157$ and larger initial amplitude modulation; open circles: lower-sideband amplitudes, filled circles: upper-sideband amplitudes. (*a*) Case SB12; (*b*) Case SB14.

of the induced mean current, and σ is the linear damping, which can be estimated from the measured experimental data.

To compare the numerical results with the measured data, Lo & Mei (1985) transformed (3.1) into a moving coordinate system with the following dimensionless variables:

$$
\left.
\begin{aligned}
A = a_0 A', &\qquad \phi = \omega_0 a_0^2 \phi', \\
\varepsilon \omega_0 \gamma \left(\frac{2k_0}{\omega_0} x - t \right) = \xi, &\qquad \varepsilon k_0 \gamma z = z', \\
\varepsilon^2 k_0 x = \eta, &\qquad \varepsilon \lambda k_0 h = h',
\end{aligned}
\right\}
\tag{3.2}
$$

where γ is scale factor which renders the computational domain of ξ into $[0, 2\pi]$. With (3.2), the normalized Dysthe's equation with a linear damping term becomes:

$$
\frac{\partial A}{\partial \eta} + i\gamma^2 \frac{\partial^2 A}{\partial \xi^2} + i|A|^2 A + 8\varepsilon\gamma |A|^2 \frac{\partial A}{\partial \xi} + 4i\varepsilon\gamma A \frac{\partial \phi}{\partial \xi} \bigg|_{z=0} + \tilde{\sigma} A = 0,
\tag{3.3}
$$

$$
\sigma_e = \varepsilon^2 k_0 \tilde{\sigma}.
\tag{3.4}
$$

For brevity, the primes in (3.3) are omitted. Without the fourth and the fifth terms, (3.3) reverts to the NLS equation for deep water.

The initial condition used in the numerical model is:

$$
A(\xi, 0) = 1 + S_{+n} \exp\left[i(\xi + \varphi_{+n})\right] + S_{-n} \exp\left[i(\xi + \varphi_{-n})\right]
\tag{3.5}
$$

where S and φ are the measured initial amplitude ratio and the relative phase, respectively, between the sidebands and the carrier waves. In this study, the first two sidebands ($n = 1, 2$) are used in the simulations. The detailed complex amplitudes for each wave component measured at the first location $x = 4.9$ m are shown in table 2.

Following Segur *et al.* (2005) and Henderson *et al.* (2010), we assume that wave energy decay is exponential:

$$
E(x) = E(0) \exp(-2\sigma_e x).
\tag{3.6}
$$

We will use σ_e to denote the dissipation rate estimated from the experimental data. The measured data are fitted using the least-squares method. Figure 10 illustrates two examples of the fitted curves for experimental cases. It can be seen that the decay can
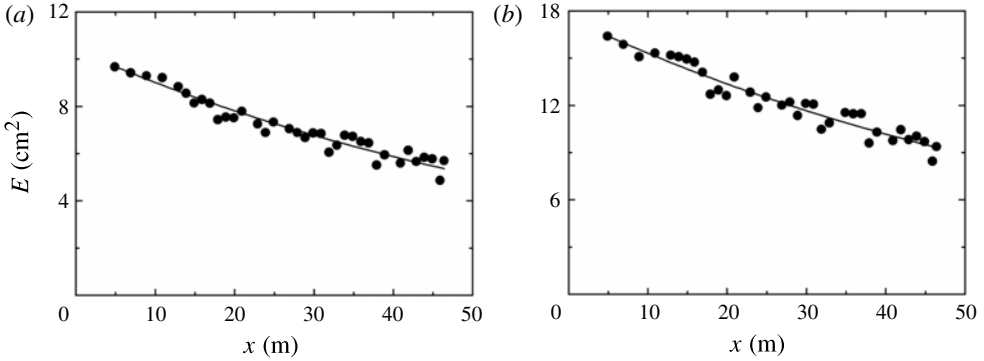
FIGURE 10. The measured E and the fitted curves: (*a*) Case SB2; (*b*) Case SB8.
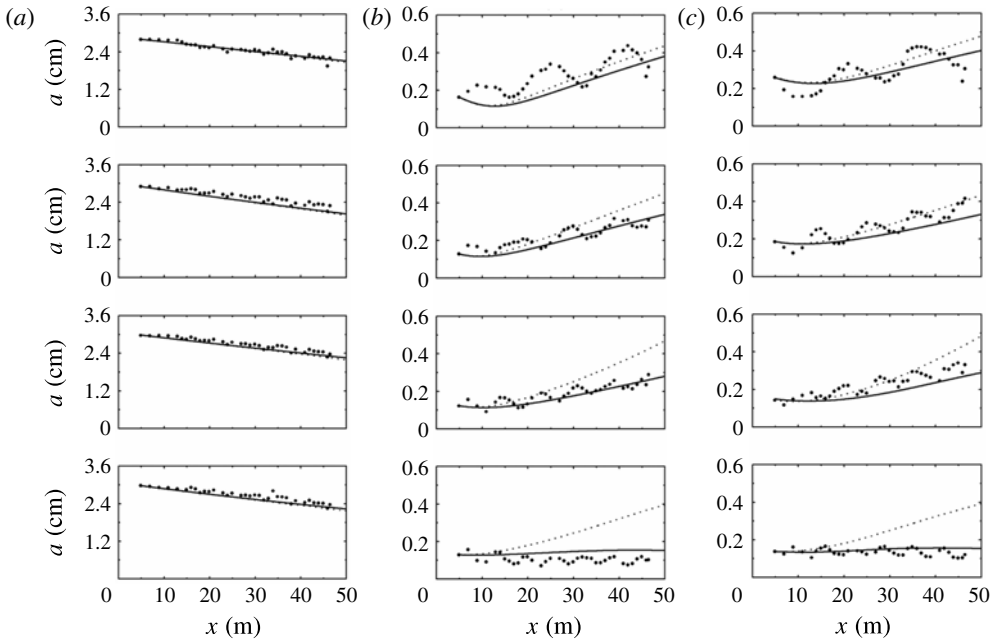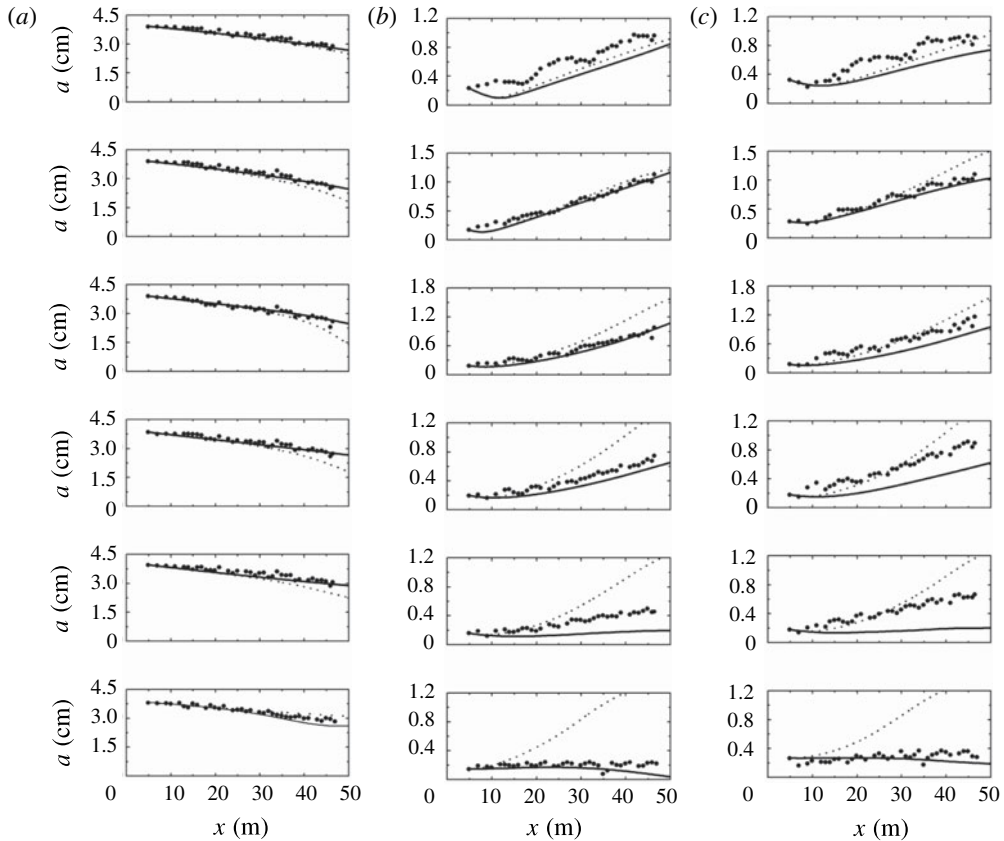

FIGURE 11. Predictions with the linear damping term from Dysthe's equation (solid lines) and the NLS equation (light dotted lines). The measured amplitudes (bold dots) are the results for the initial weakly perturbed cases with the smaller steepness: (*a*) the carrier waves a_c; (*b*) the first lower sidebands a_{-1}; (*c*) the first upper sidebands a_{+1}. Cases SB1–SB4 (top to bottom).

be described reasonably well by the exponential curve. The estimated σ_e for all the experimental cases is presented in table 1. Converting σ_e then to $\tilde{\sigma}$ using (3.4), and inserting its value in (3.3) completes the parameters required. According to Lo & Mei (1985), the linear theoretical dissipation rate due to the wall boundary layer can be written:

$$\sigma_D = \left(\frac{\nu}{\pi f_c}\right)^{1/2} \frac{k_c}{B},\qquad(3.7)$$

FIGURE 12. Predictions with the linear damping term from Dysthe's equation (solid lines) and the NLS equation (light dotted lines). The measured amplitudes (bold dots) for the initial weakly perturbed cases with the larger steepness: (*a*) the carrier waves a_c; (*b*) the first lower sidebands a_{-1}; (*c*) the first upper sidebands a_{+1}. Cases SB5–SB10 (top to bottom).

where B is the flume width, and, $\nu = 10^{-6}$ m^2 s^{-1} is the kinematic viscosity of water. For the present flume, $B = 0.8$, so that the theoretical linear dissipation rate of the experimental cases is 0.0028 m^{-1}, which is smaller than the measured σ_e. Hence, the dissipation seen in the experiments includes contributions other than those included in the theory, such as those due to contact lines and surface boundary layers.

Figure 11 presents comparisons between the measured amplitudes and the numerical results for the initial weakly perturbed wave trains with $\varepsilon = 0.115$. The results indicate that both Dysthe's and the NLS equations with a linear damping term, which is estimated from the measured data, predict well the evolution of the nonlinear wave trains with $\delta < 1.0$. However, for cases with $\delta > 1.0$ (Case SB4), Dysthe's equation predicts the evolution well, but the NLS equation clearly overestimates the sideband growth. As the higher sidebands for these cases do not exhibit obvious growth (see figure 3), the comparisons for the evolution of the sideband are not illustrated here. It is noticed that Dysthe's equation still cannot predict the oscillations of the sidebands downstream, suggesting that the oscillations may be caused by higher-order wave interactions. The agreement between the measured and the numerical results indicates
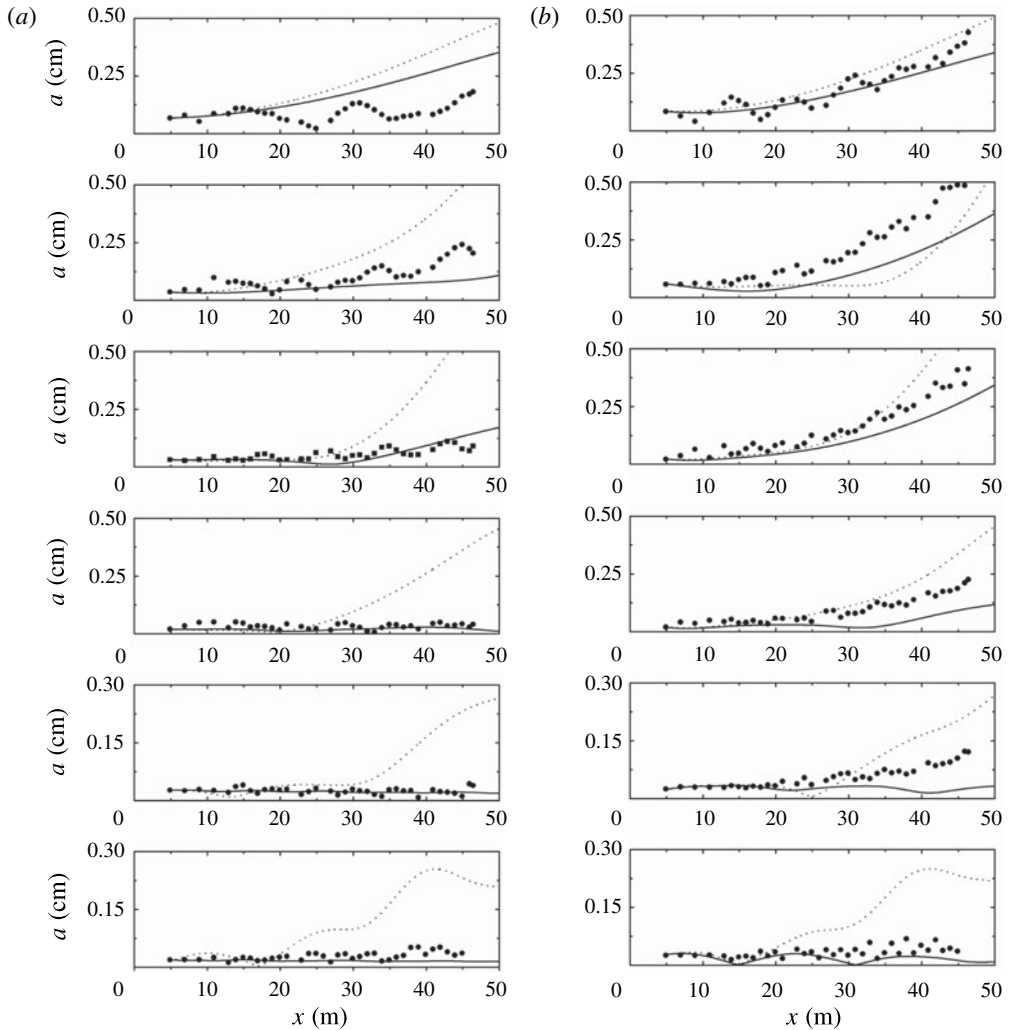
FIGURE 13. Predictions for the evolution of the second sidebands by Dysthe's equation (solid lines) and the NLS equation (light dotted lines) with the linear damping term. The measured amplitudes (bold dots) for the initial weakly perturbed cases with the larger steepness: (*a*) the second lower sidebands a_{-2}; (*b*) the second upper sidebands a_{+2}. Cases SB5–SB10 (top to bottom). Here, unlike figures 11 and 12, Cases SB1–SB4 have been omitted as they do not exhibit obvious growth.

that the dissipation effect on the modulational evolution related to the initial perturbed frequencies can also be predicted within the framework of the NLS equation.

Comparisons of the carrier wave (f_c) and the first sidebands ($f_c \pm \delta f$) are shown in figure 12 for the cases with initial weakly perturbed waves with larger initial steepness. The corresponding comparisons for the second sidebands ($f_c \pm 2\delta f$) are shown in figure 13. The results indicate that, for the cases with obvious sideband growth, the experimental Cases SB6 can be modelled reasonably well by the two numerical models. For the stabilized case (SB10), which has a broad bandwidth $\delta = 1.11$, Dysthe's equation predicts the evolution well, but the NLS equation overestimates greatly the sideband evolution. It is interesting to note that for Cases SB7–SB9,
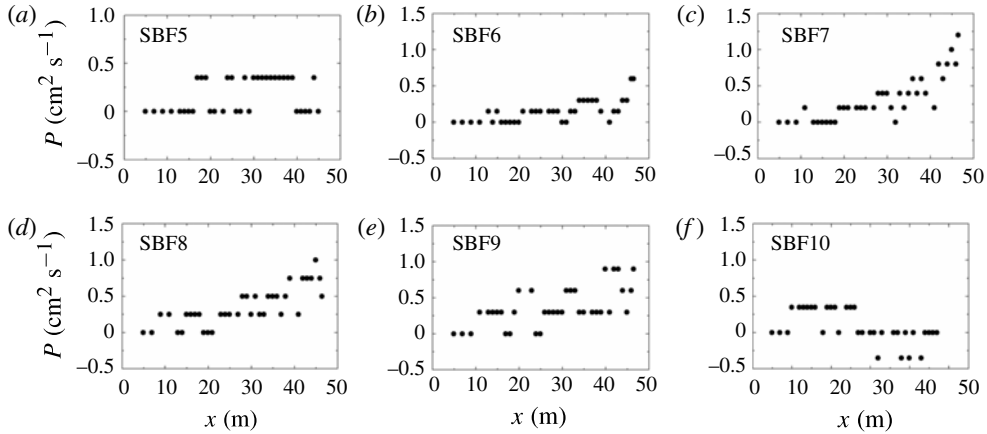
FIGURE 14. The evolution of the integral quantity P along the flume for cases corresponding to figure 12.

Dysthe's equation predicts the lower sidebands well, while the NLS equation predicts the upper sidebands better. This phenomenon also can be observed for the second-sideband evolution (figure 13).

Segur *et al.* (2005) claimed that the NLS-type equations are invalid if the integral of the 'linear momentum' P is not conserved. For experimental data, P can be defined as:

$$P = 2\Delta f \sum_{i=-n}^{n} \mathrm{i}\,|a_i|^2. \tag{3.8}$$

In this study, n is chosen as 6, indicating that only the first six sidebands are considered. The computed P for Cases SB5–SB10 is shown in figure 14. For Cases SB7–SB9, the values of P increase gradually along the tank, which is consistent with the disagreement between the measured and numerical results in the theoretical framework of Segur *et al.* (2005).

The comparisons between the numerical predictions and the measured data for the cases with initial larger perturbations are shown in figure 15. Dysthe's model predicts fairly well the evolution for Case SB11. However, the prediction from the NLS equation for this case is overestimated, mainly due to the initial frequency bandwidth ($\delta = 1.09$). For the other three cases (Cases SB12–14), both Dysthe's and the NLS equations are invalid. As the momentum integrals for these cases are not conserved during the evolution (figure 16), the discrepancies between the numerical results and the measured data are consistent with the theory of Segur *et al.* (2005). Similar to the previous cases, the integral P for this case has a tendency toward positive values. This phenomenon is caused primarily by the asymmetric growth of the lower and upper sidebands.

4. Discussion on the oscillatory growth of sidebands

In the above discussion, the evolution of the sidebands showed an oscillatory growth pattern, especially for the cases with the smaller steepness (figure 4). Although the physical mechanism of this phenomenon is unknown, the oscillation is seemingly related to the difference frequency Δf.
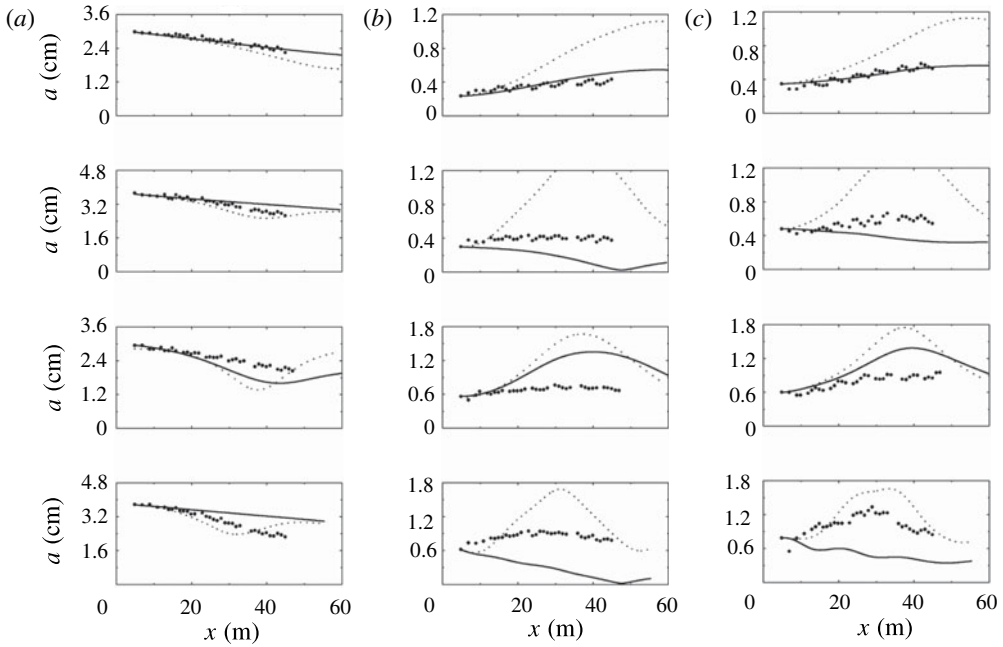
FIGURE 15. Predictions with the linear damping term using Dysthe's equation (solid lines) and the NLS equation (light dotted lines). The measured amplitudes (bold dots) for the initial large perturbed cases: (*a*) the carrier waves a_c; (*b*) the first lower sidebands a_{-1}; (*c*) the first upper sidebands a_{+1}. Cases SB11–SB14 (top to bottom).

From the measured data, the evolution of the sidebands can be assumed to be composed of two parts. One part is the exponential growth/decay or trend in the data, the other is the oscillation which is assumed to have constant amplitude. Hence, the development of the sidebands can be modelled by:

$$a(kx) = a(0)\exp(\beta_x kx) + \tilde{a}\cos(\tilde{K}kx), \qquad (4.1)$$

where $\tilde{a}$ is the oscillation amplitude and $\tilde{K}k$ is the wavenumber of the oscillation. Then, $\tilde{a}$ and $\tilde{K}$ can be estimated through fitting data to (4.1) by adopting the least-squares method. The fitted results for the first four cases are shown in figure 17. It can be seen that the above equation models the sideband evolution quite well.

More interestingly, table 3 presents the estimated parameters required by (4.1) where it is found that the oscillation wavenumber multiplier $\tilde{K}$ is very close to K/k, where K is the difference wavenumber. As illustrated in figure 17, by replacing $\tilde{K}$ in (4.1) with K, the curves model the growth well. Thus, the second term of (4.1) can be written approximately as $\tilde{a}\cos(Kx)$, which also demonstrates the appropriateness of the assumption that the oscillation is related to the disturbance frequency.

5. Conclusions

New experiments focused on the effects of dissipation on the Benjamin–Feir instability have been conducted. In this study, dissipation is caused primarily by the background environment of the tank. A number of wave trains with varying initial steepness, perturbation frequency and initial perturbed strength are mechanically
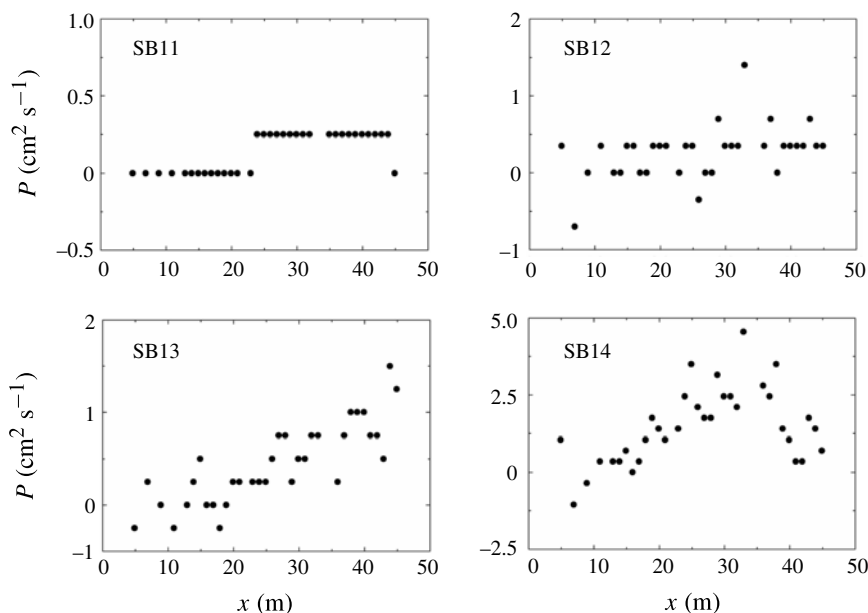
FIGURE 16. The evolution of the integral quantity P along the flume for cases with initial large perturbations.

Case	Δf (Hz)	K/k	a_{+1} (cm)	$\tilde{K}_{+1}$	a_{-1} (cm)	$\tilde{K}_{-1}$
SB1	0.05	0.10	0.0568	0.1056	0.061	0.0967
SB2	0.075	0.15	0.0265	0.1591	0.039	0.1523
SB3	0.1	0.20	0.0263	0.1954	0.023	0.2045
SB4	0.125	0.25	0.0239	0.2439	0.021	0.2409

TABLE 3. The estimated parameters required by (4.1)

generated in a long wave flume. The primary results of the present experiments show that even though perturbations grow somewhat, the growth is bounded, confirming the stabilization theory of Segur *et al.* (2005) directly. By increasing the perturbed amplitudes, the stabilization effect can be mitigated partially, but the ability to affect stabilization is limited, especially for the lower sidebands. It is also found that the effect of dissipation is related closely to the perturbation frequency. Even with a similar theoretical growth rate, wave trains with higher perturbed frequencies are easier to stabilize in the presence of dissipation. However the physical mechanism responsible for this phenomenon has not been determined. In addition, the growth rate of waves with larger amplitudes is reduced further by dissipation than waves with smaller amplitudes.

Numerical simulations have been performed using both Dysthe's equation and the NLS equation with a linear exponential damping term, which is estimated through fitting the measured data. The initial condition for the numerical models is obtained from the first measurement location. The results indicate that both equations can predict reasonably well the evolution of the wave trains if the momentum integral of
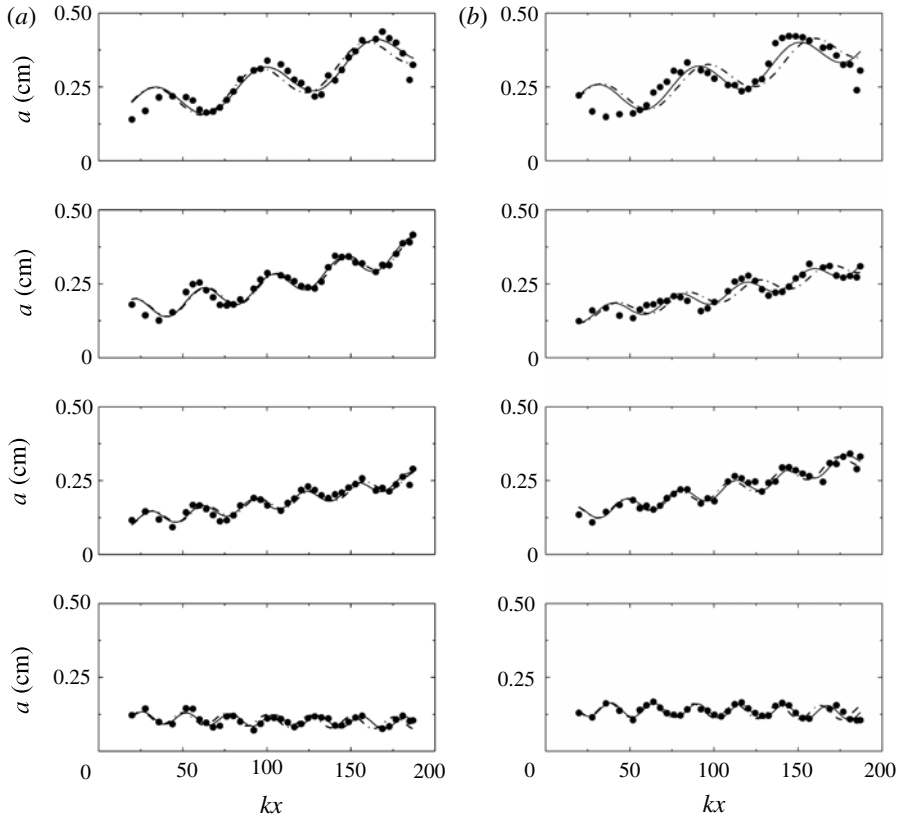
FIGURE 17. The fitted curves of the sideband evolution for the first four cases using (4.1) (Cases SB1–SB4, top to bottom): bold dots represent the measured data, the solid curves are the fitted results using (4.1), the dash dot lines represent the results by replacing $\tilde{K}$ with K in (4.1). (*a*) The first lower sidebands a_{-1}, (*b*) the first upper sidebands a_{+1}.

the wave trains is conserved during the evolution. However Dysthe's equation performs better than the NLS equation for cases with higher perturbation frequency.

Acknowledgements

REFERENCES

ALBER, I. E. 1978 The effects of randomness on the stability of two-dimensional surface wavetrains. *Proc. R. Soc. Lond.* A **363**, 525–546.

BANNER, M. L. & PEIRSON, W. L. 2007 Wave breaking onset and strength for two-dimensional deep-water wave groups. *J. Fluid Mech.* **585**, 93–115.

BENJAMIN, T. B. 1967 Instability of periodic wavetrains in nonlinear dispersive systems. *Proc. R. Soc. Lond.* A **299**, 59–75.

BENJAMIN, T. B. & FEIR, J. E. 1967 The disintegration of wave trains on deep water. Part I. Theory. *J. Fluid Mech.* **27**, 417–430.

CANNEY, N. E. & CARTER, J. 2007 Stability of plane waves on deep water with dissipation. *Math. Comput. Simul.* **74**, 159–167.

CARTER, J. D. & CONTRERAS, C. C. 2008 Stability of plane-wave solutions of a dissipative generalization of the nonlinear Schrodinger equation. *Physica* D **237** (24), 3292–3296.

CHIANG, W. S. & HWUNG, H. H. 2007 Steepness effect on modulation instability of the nonlinear wave train. *Phys. Fluids* **19**, 1–13.

DYSTHE, K. 1979 Note on a modification to the nonlinear Schrödinger equation for application to deep water waves. *Proc. R. Soc. Lond.* A **369**, 105–114.

GRAMSTAD, O. & TRULSEN, K. 2011 Hamiltonian form of the modified nonlinear Schrödinger equation for gravity waves on arbitrary depth. *J. Fluid Mech.* **670**, 404–426.

HAMMACK, J. L. & HENDERSON, D. M. 1993 Resonant interactions among surface-water waves. *Annu. Rev. Fluid Mech.* **25**, 55–97.

HENDERSON, D. M., SEGUR, H. & CARTER, J. D. 2010 Experimental evidence of stable wave patterns on deep water. *J. Fluid Mech.* **658**, 247–278.

HWUNG, H. H., CHIANG, W. S. & HSIAO, S. C. 2007 Observations on the evolution of wave modulation. *Proc. R. Soc. Lond.* A **463** (2077), 85–112.

ISLAS, A. & SCHOBER, C. M. 2011 Rogue waves, dissipation, and downshifting. *Physica* D **240** (12), 1041–1054.

JANSSEN, P. A. E. M. 2003 Nonlinear four wave interaction and freak waves. *J. Phys. Oceanogr.* **33**, 863–884.

KHARIF, C., KRAENKEL, R. A., MANNA, M. A. & THOMAS, R. 2010 The modulational instability in deep water under the action of wind and dissipation. *J. Fluid Mech.* **664**, 138–149.

KRASITSKII, V. P. 1994 On reduced equations in the Hamiltonian theory of weakly nonlinear surface waves. *J. Fluid Mech.* **272**, 1–20.

LAKE, B. M., YUEN, H. C., RUNGALDIER, H. & FERGUSON, W. E. 1977 Nonlinear deep-water waves – theory and experiment. Part 2. Evolution of a continuous wave train. *J. Fluid Mech.* **83** (November), 49–74.

LO, E. & MEI, C. C. 1985 A numerical study of water-wave modulation based on a higher-order nonlinear Schrödinger-equation. *J. Fluid Mech.* **150**, 395–416.

MEI, C. C. & HANCOCK, M. J. 2003 Weakly nonlinear surface waves over a random seabed. *J. Fluid Mech.* **475**, 247–268.

MELVILLE, W. K. 1982 The instability and breaking of deep-water waves. *J. Fluid Mech.* **115**, 165–185.

SEGUR, H., HENDERSON, D., CARTER, J., HAMMACK, J., LI, C., PHEIFF, D. & SOCHA, K. 2005 Stabilizing the Benjamin–Feir instability. *J. Fluid Mech.* **539**, 229–271.

TIAN, Z., PERLIN, M. & CHOI, W. 2010 Energy dissipation in two-dimensional unsteady plunging breakers and an eddy viscosity model. *J. Fluid Mech.* **655**, 217–257.

TOUBOUL, J. & KHARIF, C. 2010 Nonlinear evolution of the modulational instability under weak forcing and damping. *Nat. Haz. Earth Syst. Sci.* **10** (12), 2589–2597.

TRULSEN, K. & DYSTHE, K. B. 1996 A modified nonlinear Schrodinger equation for broader bandwidth gravity waves on deep water. *Wave Motion* **24** (3), 281–289.

TULIN, M. P. & WASEDA, T. 1999 Laboratory observations of wave group evolution, including breaking effects. *J. Fluid Mech.* **378**, 197–232.

WASEDA, T. & TULIN, M. P. 1999 Experimental study of the stability of deep-water wave trains including wind effects. *J. Fluid Mech.* **401**, 55–84.

WU, G. Y., LIU, Y. M. & YUE, D. K. P. 2006 A note on stabilizing the Benjamin–Feir instability. *J. Fluid Mech.* **556**, 45–54.

YUEN, H. C. & LAKE, B. M. 1980 Instabilities of waves on deep-water. *Annu. Rev. Fluid Mech.* **12**, 303–334.

ZAKHAROV, V. E. 1968 Stability of periodic waves of finite amplitude on the surface of deep fluid. *J. Appl. Mech. Tech. Phys.* **9** (2), 19.